Supporting information

Engineering $CoMnO_x$ nanocube core catalyst by epitaxial growth of $CoAlO_x$ hydrotalcite shell nanosheets for efficient elimination of propane

Shixing Wu[a,b#], Shilin Wu[d#], Fang Dong[a], Siyi Ma[a,b], Yu Meng[e*], Haitao Zhang[c], Zhicheng Tang[a*]

([a] National Engineering Research Center for Fine Petrochemical Intermediates, State Key Laboratory for Oxo Synthesis and Selective Oxidation, Lanzhou Institute of Chemical Physics, Chinese Academy of Sciences, Lanzhou 730000, China.

[b] University of Chinese Academy of Sciences, Beijing 100039, China.

[c] Lanzhou Petrochemical Research Center, Petrochemical Research Institute, PetroChina, Lanzhou 730060, China.

[d] College of Architecture and Environment, Sichuan University, Chengdu 610065, China.

[e] Shanxi Key Laboratory of Low metamorphic Coal Clean Ytilization, School of Chemistry and Chemical Engineering, Yulin University, YuLin 719000, China.)

[#]These authors contributed equally: Shixing Wu, Shilin Wu.

---

[*]Corresponding author.

E-mail address: tangzhicheng@licp.cas.cn (Z. Tang), mengyu@yulinu.edu.cn (Y. Meng).

1. The details of reagents and materials

Chemical materials in this work are all analytical grade reagents and directly used to prepare catalysts without further treatment. Prussian blue analogue (PBA) of $Mn_3[Co(CN)_6]_2 \cdot nH_2O$ nanocubes were synthesized via a self-assemble route. Analytical grade vinylpyrrolidone (PVP), Manganese acetate tetrahydrate, Potassium cobalt cyanide, Cobalt nitrate hexahydrate and Aluminum nitrate nine-water were purchased from Shanghai Aladdin Reagent Co. Ltd, China.

2. Catalyst characterizations

The morphology of the catalyst samples was analyzed by transmission electron microscopy (TEM, JEOL-JEM-2010). Scanning electron microscope (SEM) images of the samples were obtained by a JSM-6701F cold field emission scanning electron microscope. The crystal phases of each element in the catalyst were determined by an X-ray diffraction instrument (XRD, Japan Smartlabse) (scanning angle of 10°-90°, scanning speed of 0.5 °/min, 60 kV, 55 mA) under the radiation of λ=1.5406 nm. The Fourier transform infrared spectroscopy (FTIR) analysis of the samples was performed using a Fourier infrared spectrometer (Nexus 870, Nicolet), and ATR technology was used for FTIR analysis. Brunauer-Emmett-Teller (BET) surface area, the pore size, and the pore volume of the catalysts were obtained by adsorption and desorption of nitrogen in the ASAP 2020 instrument (America Micromeritics). The real content of each metal on the catalyst was obtained by measuring each catalyst with an Agilent ICP-OES 730 instrument. Infrared spectra were tested with a Nicolet Nexus 870 Fourier transform

infrared spectrometer. X-ray photoelectron spectroscopy (XPS) measurements were performed with a Thermo Scientific 250 Xi.

The multifunctional dynamic adsorption instrument TP-5080-D was used to analyze the acidity and redox capacity of the catalyst surface. For H_2-TPR, a 50 mg sample was heated from room temperature to 900 ^oC in reduced gas with volume fractions of 5 vol % H_2 and 95 vol % N_2, and the detector signal was continuously recorded. For the O_2-TPD test, the catalyst (50 mg) was pretreated with nitrogen (99.9%) for 1 h at 300 ^oC. When the temperature dropped to 50 ^oC, the O_2 (5% O_2/N_2) adsorption was carried out for 60 min. After the adsorption was over, purged for 0.5 h, and the desorbed O_2 signal was detected at 50-900 ^oC. The temperature-programmed desorption operation of NH_3-TPD was similar to that of O_2-TPD, except that O_2 was changed to NH_3. For the C_3H_8-TPD experiments, samples (50 mg) were pretreated in an N_2 stream (30 mL/min) for 30 min at 300 ^oC. The catalysts were then exposed to 5 vol% C_3H_8/Ar (40 mL/min) for 1 h, followed by a N_2 purge for 15 min. Finally, the catalysts were purged in a stream of $CoMnO_x$ (40 mL/min) from 50-400 ^oC (10 ^oC/min) to start the temperature increase.

3. Catalytic activity measurements

The activity and stability of the catalysts were tested with the help of propane (C_3H_8) as a probe molecule, which was essential for the study of the catalytic oxidation performance of VOCs. By pressing and sieving (40-60 mesh), it was possible to obtain 0.4 g of sample, to which 0.2 g of silica (SiO_2) was subsequently added. The catalyst and SiO_2 were mixed well and poured into the constant temperature zone of a

continuous flow microreactor tube (length of 30 cm, 8 mm of inner diameter), which was stuffed with cotton. The catalyst was exposed to a mixture of C_3H_8 (2000 ppm) and the air with a flow rate of 200 mL/min and a weight hourly space velocity (WHSV) of 30000 $mL \cdot g^{-1} \cdot h^{-1}$. An on-line gas chromatograph (FULI, GC9790II) equipped with a flame ionization detector (FID) was used to detect the concentration of the reactants. Usually, the activity was distinguished by the reaction temperature when the C_3H_8 conversion was 90%. The conversion efficiency of C_3H_8 was calculated by the following equation:

$$x = \frac{C_{in} - C_{out}}{C_{in}} \times 100\%$$

Where x is the conversion of C_3H_8, C_{in} and C_{out} are the inlet and outlet concentrations of C_3H_8 in the gas phase.

4. DFT measurement

All theoretical calculations in this paper are performed by Vienna Ab Initio Simulation Package (VASP) calculation software based on density functional theory. Among them, the standard projected augment plane-wave (PAW) pseudopotential of each element is selected. After the energy convergence test, the Cut-off energy is 450 eV. In order to more accurately describe the orbital electron distribution of each element, all calculations take into account the spin polarization of the electron. In addition, for all self-consistent calculations, the standard convergence thresholds for energy and force are 10-5 eV and 0.02 eV/Å, respectively. For Brillouin region integration, the sampling scheme is Monkhorst-Pack scheme with sampling density of 0.03×2π/Å.

5. In-situ FTIR measurement

In-situ diffuse reflectance infrared Fourier transform spectroscopy (DRIFTS) spectra was collected with VERTEX 70 spectrometer equipped with an MCT detector and a CaF_2 window in-situ cell. DRIFTS cell was used as the reaction chamber and the spectra were collected in the frequency range of 4000-600 cm^{-1}. 200 mg grain catalyst (40-60 mesh) was packed in DRIFTS cell. For C_3H_8 adsorption spectra, the $CoMnO_x$ and $CoMnO_x@Co_1Al_1$ catalysts were pretreated at 400 °C by flowing Ar for 40 min. After the temperature cooled to 100 °C, it was exposed to 1000 ppm C_3H_8/Ar feed at a flow rate of 25 mL/min, and the adsorption was saturated. Subsequently, the adsorption saturation was reached at different temperatures (100 °C, 150 °C, 200 °C, 250 °C, 300 °C and 350 °C). For the oxidation of C_3H_8, the $CoMnO_x$ and $CoMnO_x@Co_1Al_1$ catalysts were treated with air, and then the 1000 ppm C_3H_8 in Ar was pre-adsorbed on the clean samples at 50 °C for 25 min. Subsequently, the air with a flow of 25 mL/min was poured and the in-situ DRIFTS spectra were collected at different temperature with a heating rate of 10 °C/min.

6. Kinetic studies

The catalytic performance could also be identified by kinetic studies, such as apparent activation energy (E_a), which was measured as follows:

$$\ln r = \frac{-E_a}{RT} + C \tag{1}$$

In equation (1), r represented the reaction rate ($mol \cdot s^{-1}$), T referred to the reaction temperatures, and C was a constant term.

$$r = \frac{F \times X_{Propane}}{W} \tag{2}$$

In equation (2), $X_{Propane}$ denoted the conversion of C_3H_8, F indicated the feeding rate ($mol \cdot s^{-1}$), and W corresponded to the mass of the catalyst. Therefore, the plots of lnr and 1000/T yielded the E_a value.

The kinetic studies also included specific reaction rates, such as the catalyst's mass (R_m) and catalyst's specific surface area (R_s) which was calculated required the following equation:

$$R_m = \frac{F \times \eta_{Propane}}{W} \tag{3}$$

$$R_s = \frac{F \times \eta_{Propane}}{S} \tag{4}$$

$$\eta_{Propane} = \log \frac{1}{1 - \frac{X_{Propane}}{100}} \tag{5}$$

Turnover frequency (TOF), defined as the number of C_3H_8 molecules converted per active site per second, is calculated according to the equation:

$$\text{TOF} = \frac{F_{propane} * X_{propane}}{\frac{\left(x(Co^{3+}) * x(Co)\right) + \left(x(Mn^{4+}) * x(Mn)\right)}{M_{Cat}} * m_{Cat}} \tag{6}$$

Where $F_{propane}$ is the C_3H_8 flow rate (mol/s), X_T is the conversion of C_3H_8, m_{cat} is the mass of the catalyst (g), M_{Cat} (g) is the malar of the catalysts, $x(Co^{3+})$ and $x(Mn^{4+})$ are the ratios of Co^{3+}/Co_{total} and $Mn^{4+}/(Mn^{2+}+Mn^{3+})$, respectively; x(Co) and x(Mn) are the total contents of Co and Mn in various samples (obtained by XPS experiments), respectively.

Fig. S1. Schematic diagram of the synthesis process for $CoMnO_x$ and $CoMnO_x@Co_xAl_1$ catalysts.

Fig. S2. SEM images of (a) $CoMnO_x$, (b) $CoMnO_x@Co_0Al_1$, (c) $CoMnO_x@Co_1Al_1$, (d) $CoMnO_x@Co_2Al_1$, (e) CoAl-LDH and (f) $CoMnO_x/Co_1Al_1$.

Fig. S3. SEM images and EDS element mapping of CoAl-LDH.

Fig. S4. SEM images and EDS element mapping of (a) $CoMnO_x@Co_1Al_1$ and (b) $CoMnO_x/Co_1Al_1$.

Fig. S5. TEM images of (a) $CoMnO_x$, (b) $CoMnO_x@Co_1Al_1$ and (c) $CoMnO_x@Co_3Al_1$.

Fig. S6. XRD profiles of prepared $CoMnO_x@Co_2Al_1$ material.

Fig. S7. Mapping analysis of (a-d) $CoMnO_x$.

Fig. S8. CO_2 selectivity profiles of prepared catalysts.

Fig. S9. Apparent activation energy with 5vol. H_2O of modified materials.

Fig. S10. (a and b) TG-DSC analysis of $CoMnO_x$ and $CoMnO_x@Co_1Al_1$ catalysts.

Fig. S11. XPS spectra of (a) $CoMnO_x$, (b) $CoMnO_x@Co_1Al_1$ and (c) Al 2p of $CoMnO_x@Co_xAl_1$.

Fig. S12. (a) Apparent activation energy and catalytic activity versus active metal species; (b) Catalytic activity and lattice oxygen.

Fig. S13. O_2-TPD profiles of prepared catalysts.

Fig. S14. (a) C_3H_8-TPD profiles of prepared catalysts; (b-e) TPSR studies of C_3H_8 catalytic destruction for C_3H_8 (m/z = 29), CO (m/z = 28), CO_2 (m/z = 44) and H_2O (m/z = 18).

Fig. S15. (a and b) In-situ FTIR spectra for C_3H_8 adsorption of $CoMnO_x$ catalyst for different temperatures and (c-f) oxidation C_3H_8 at air on the $CoMnO_x$.

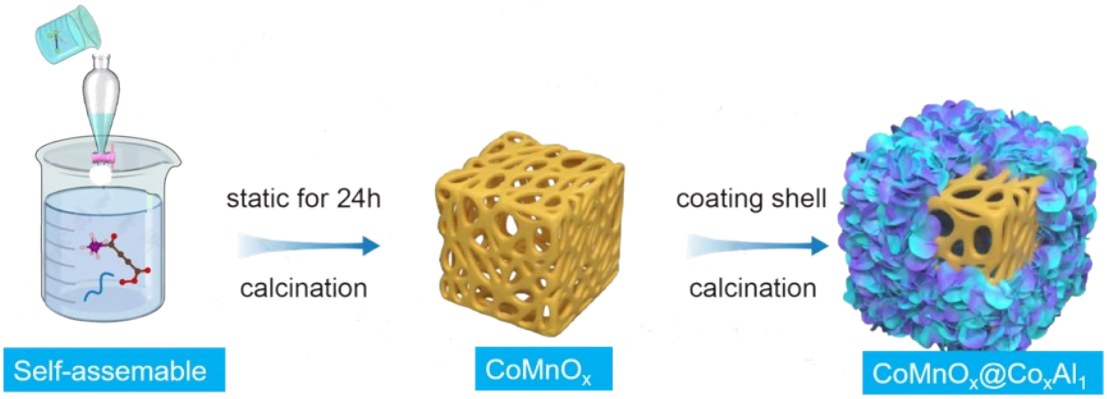

Fig. S1. Schematic diagram of the synthesis process for $CoMnO_x$ and $CoMnO_x@Co_xAl_1$ catalysts.

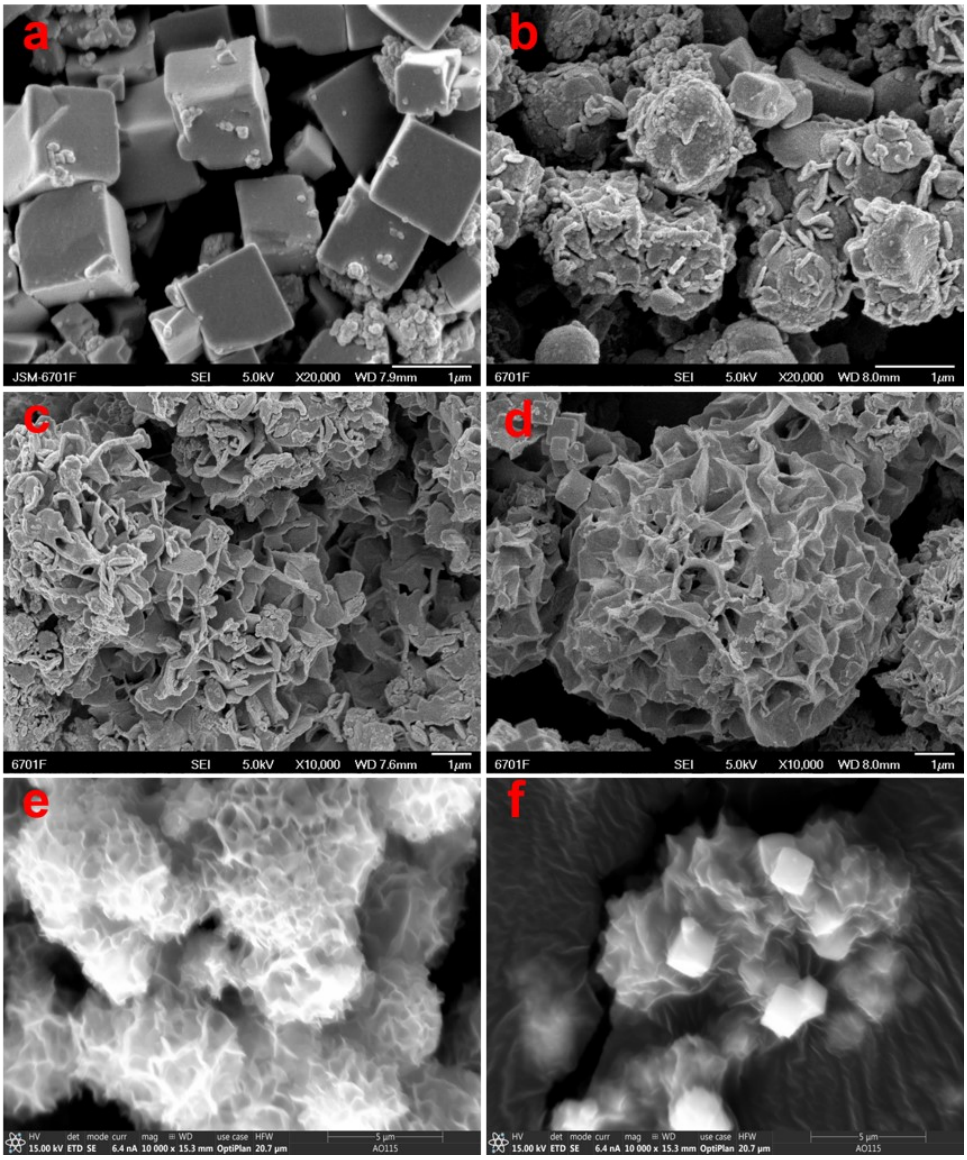

Fig. S2. SEM images of (a) $CoMnO_x$, (b) $CoMnO_x@Co_0Al_1$, (c) $CoMnO_x@Co_1Al_1$, (d) $CoMnO_x@Co_2Al_1$, (e) CoAl-LDH and (f) $CoMnO_x/Co_1Al_1$.

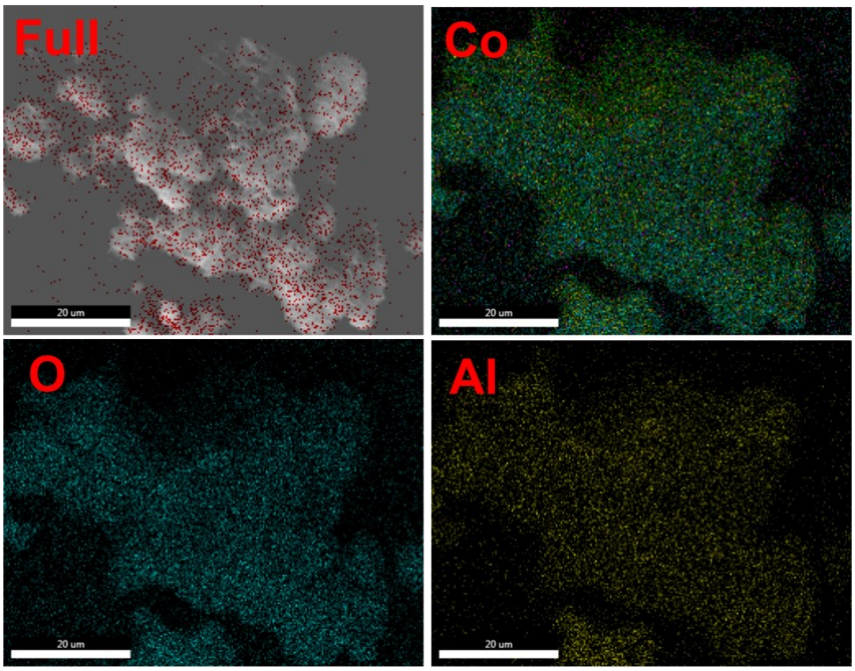

Fig. S3. SEM images and EDS element mapping of CoAl-LDH.

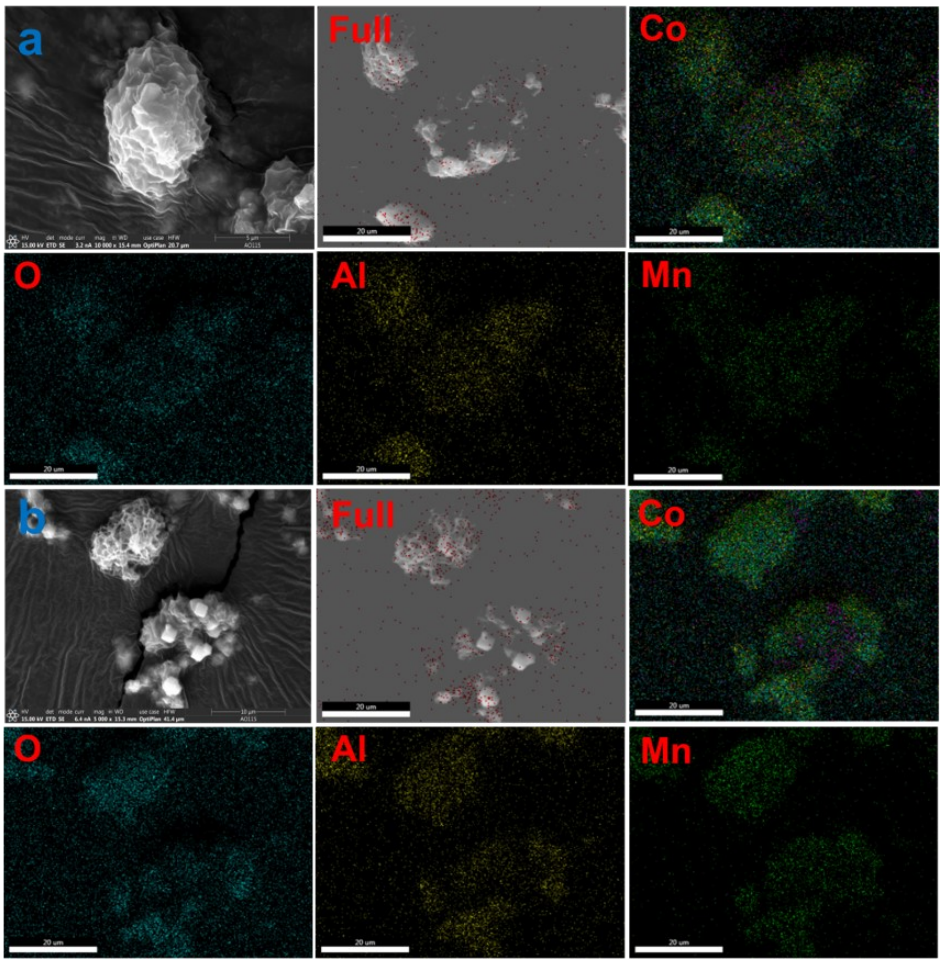

Fig. S4. SEM images and EDS element mapping of (a) $CoMnO_x@Co_1Al_1$ and (b) $CoMnO_x/Co_1Al_1$.

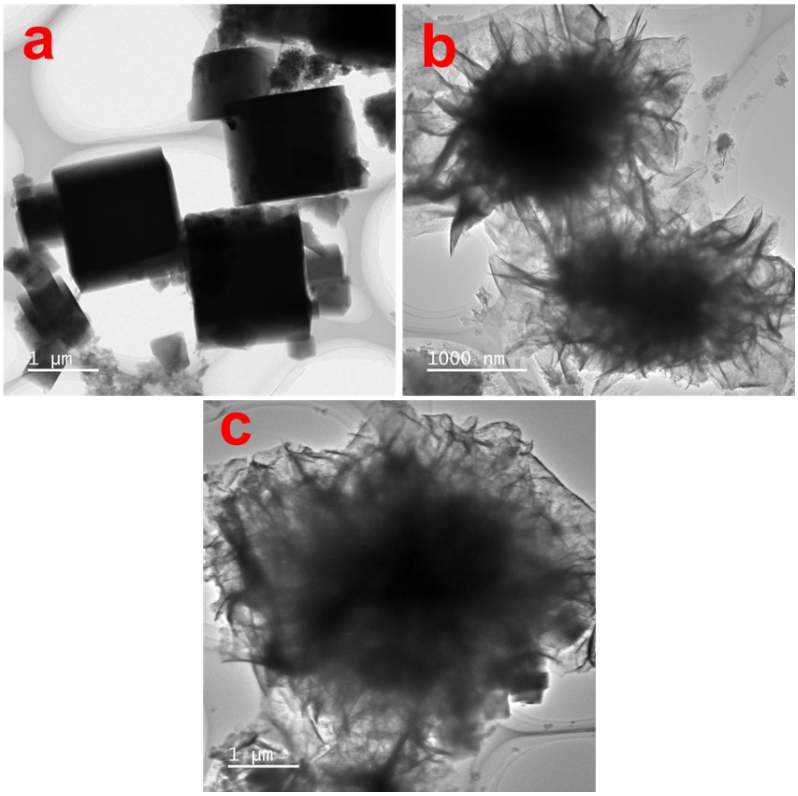

Fig. S5. TEM images of (a) $CoMnO_x$, (b) $CoMnO_x@Co_1Al_1$ and (c) $CoMnO_x@Co_3Al_1$.

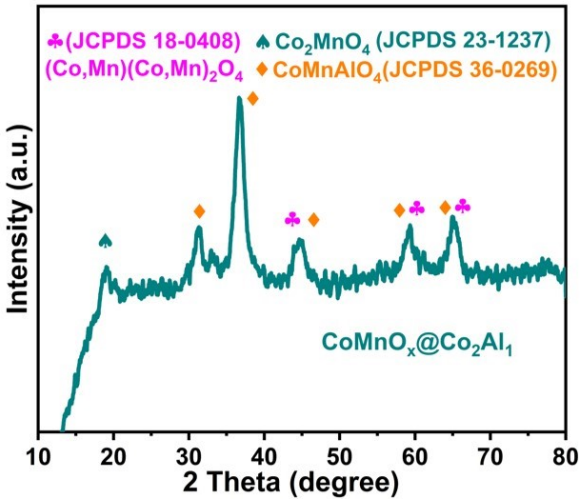

Fig. S6. XRD profiles of prepared $CoMnO_x@Co_2Al_1$ material.

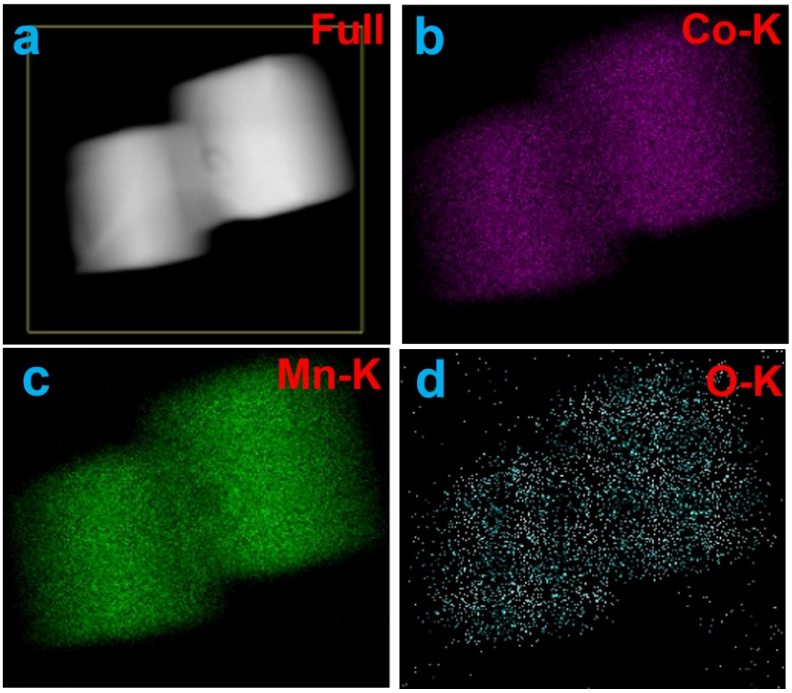

Fig. S7. Mapping analysis of (a-d) $CoMnO_x$.

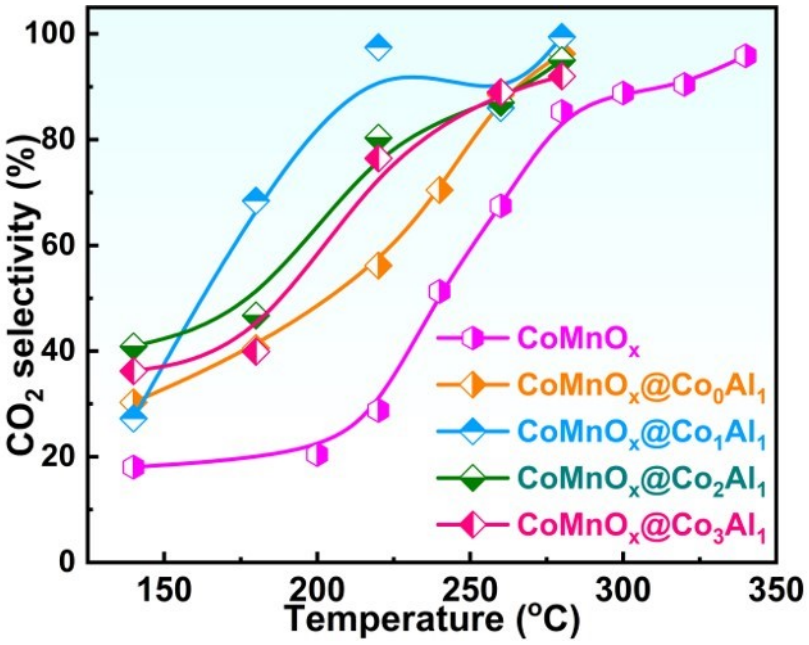

Fig. S8. CO_2 selectivity profiles of prepared catalysts.

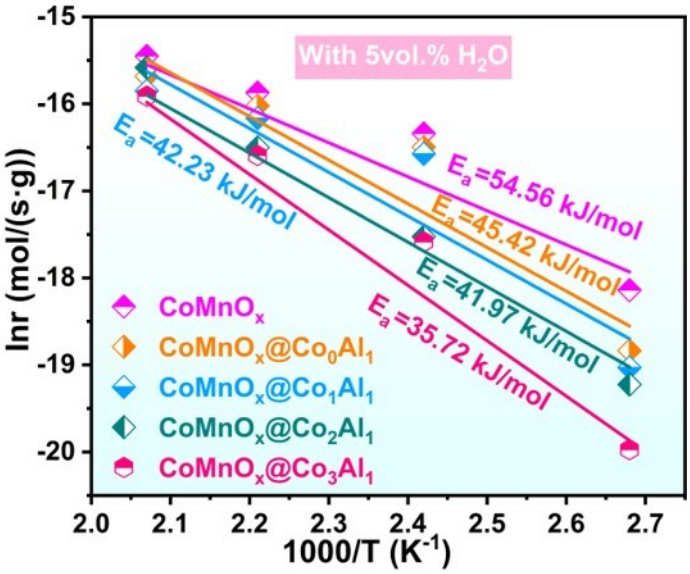

Fig. S9. Apparent activation energy with 5vol.% H_2O of modified materials.

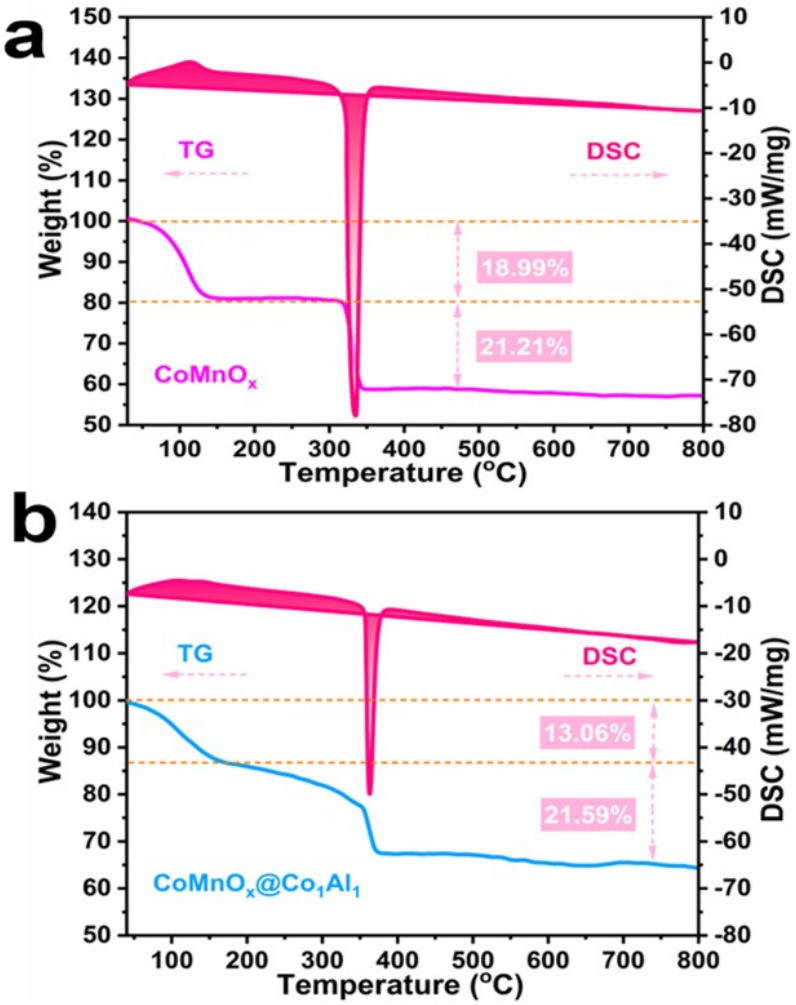

Fig. S10. (a and b) TG-DSC analysis of $CoMnO_x$ and $CoMnO_x@Co_1Al_1$ catalysts.

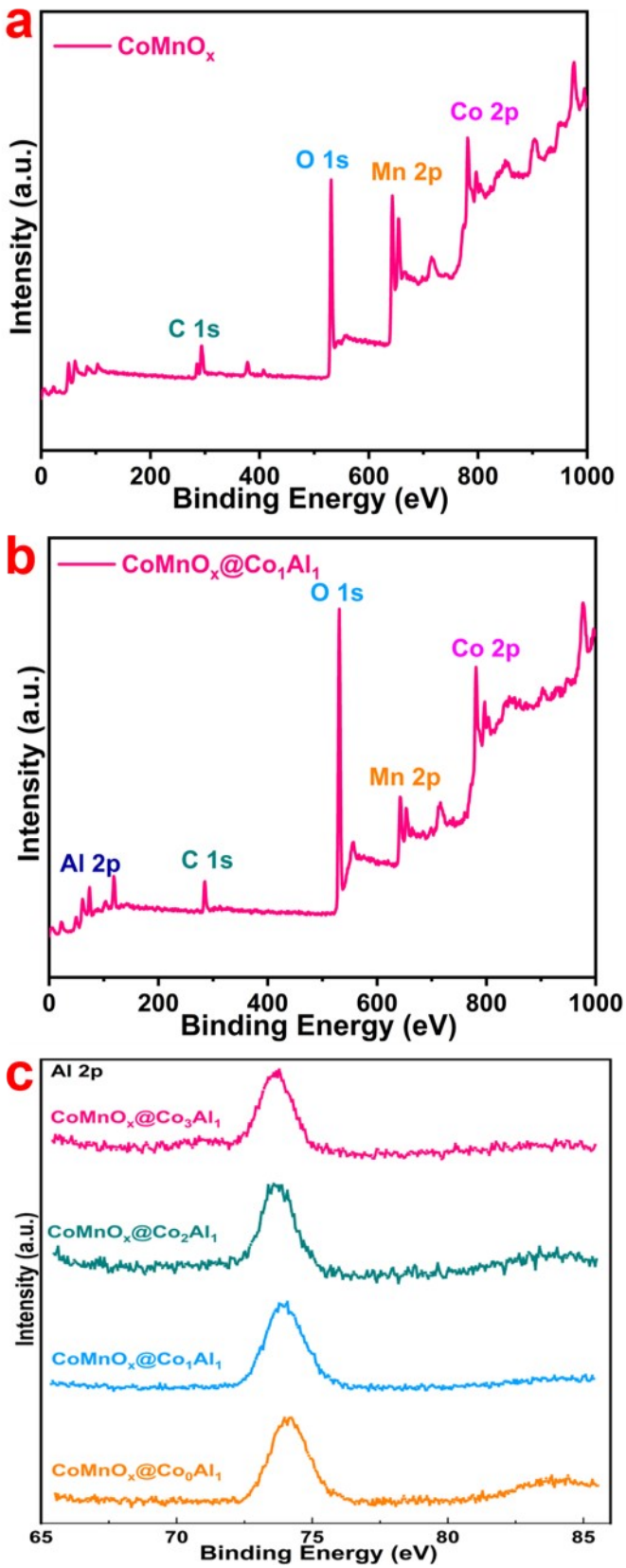

Fig. S11. XPS spectra of (a) $CoMnO_x$, (b) $CoMnO_x@Co_1Al_1$ and (c) Al 2p of $CoMnO_x@Co_xAl_1$.

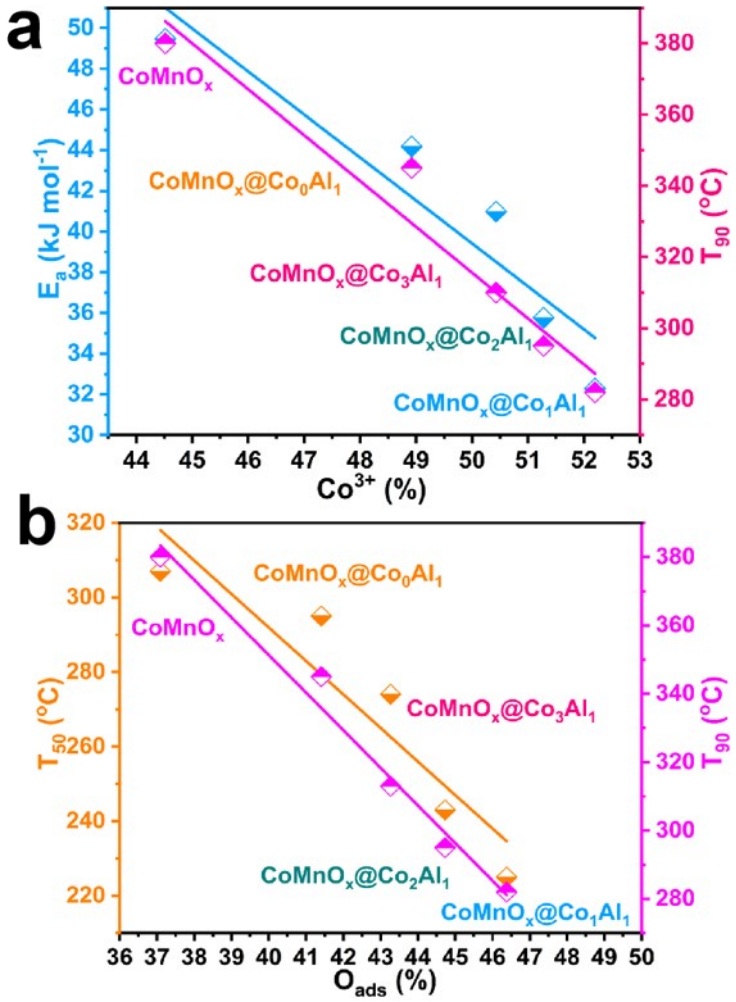

Fig. S12. (a) Apparent activation energy and catalytic activity versus active metal species; (b) Catalytic activity and adsorbed oxygen.

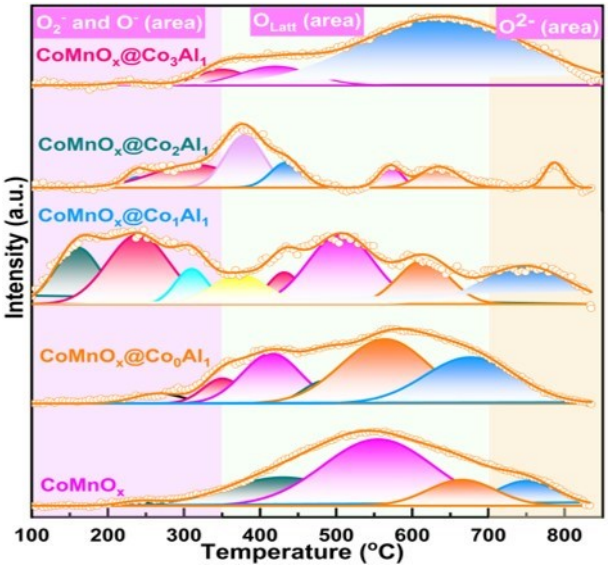

Fig. S13. O_2-TPD profiles of prepared catalysts.

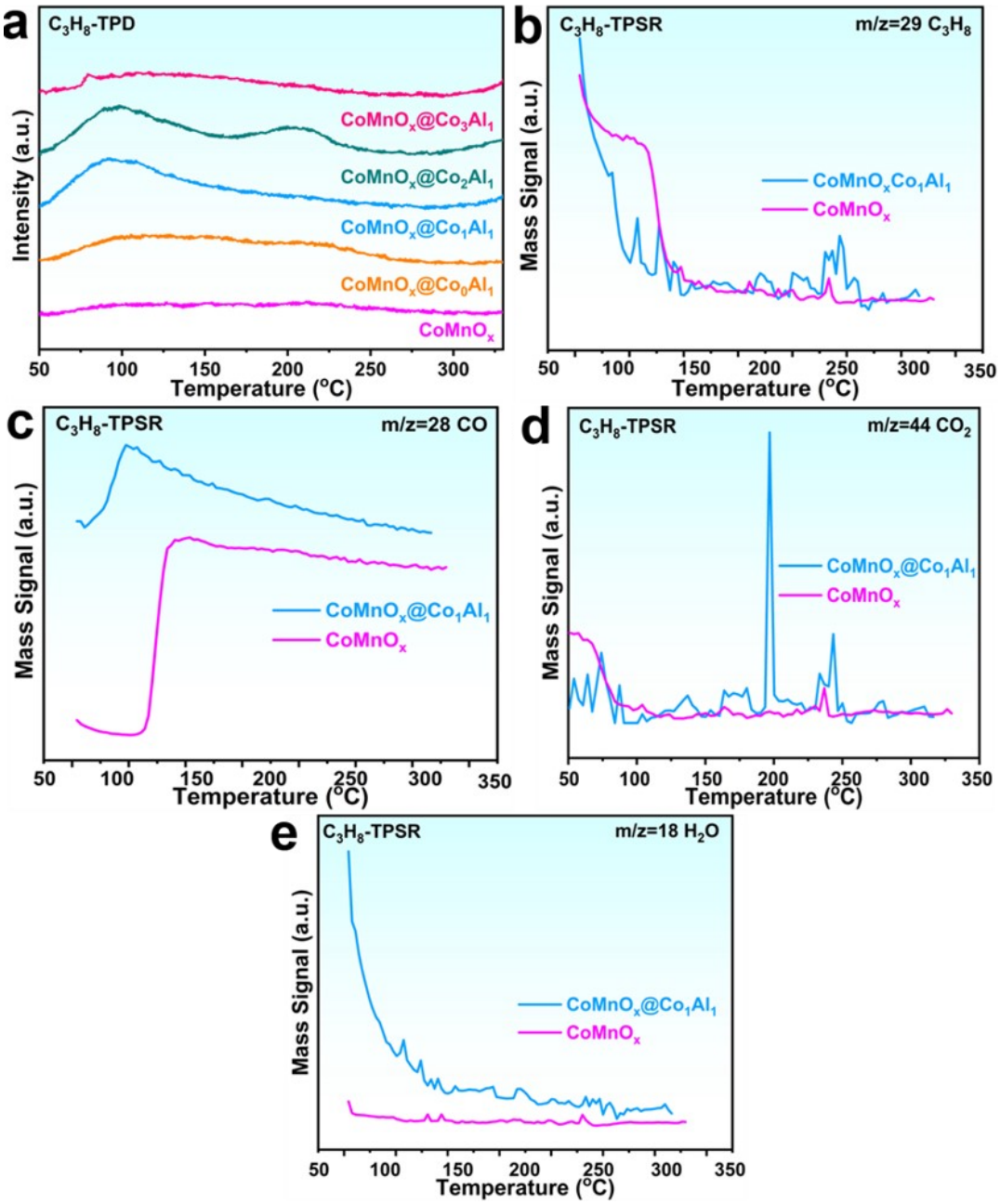

Fig. S14. (a) C_3H_8-TPD profiles of prepared catalysts; (b-e) TPSR studies of C_3H_8 catalytic destruction for C_3H_8 (m/z = 29), CO (m/z = 28), CO_2 (m/z = 44) and H_2O (m/z = 18).

.

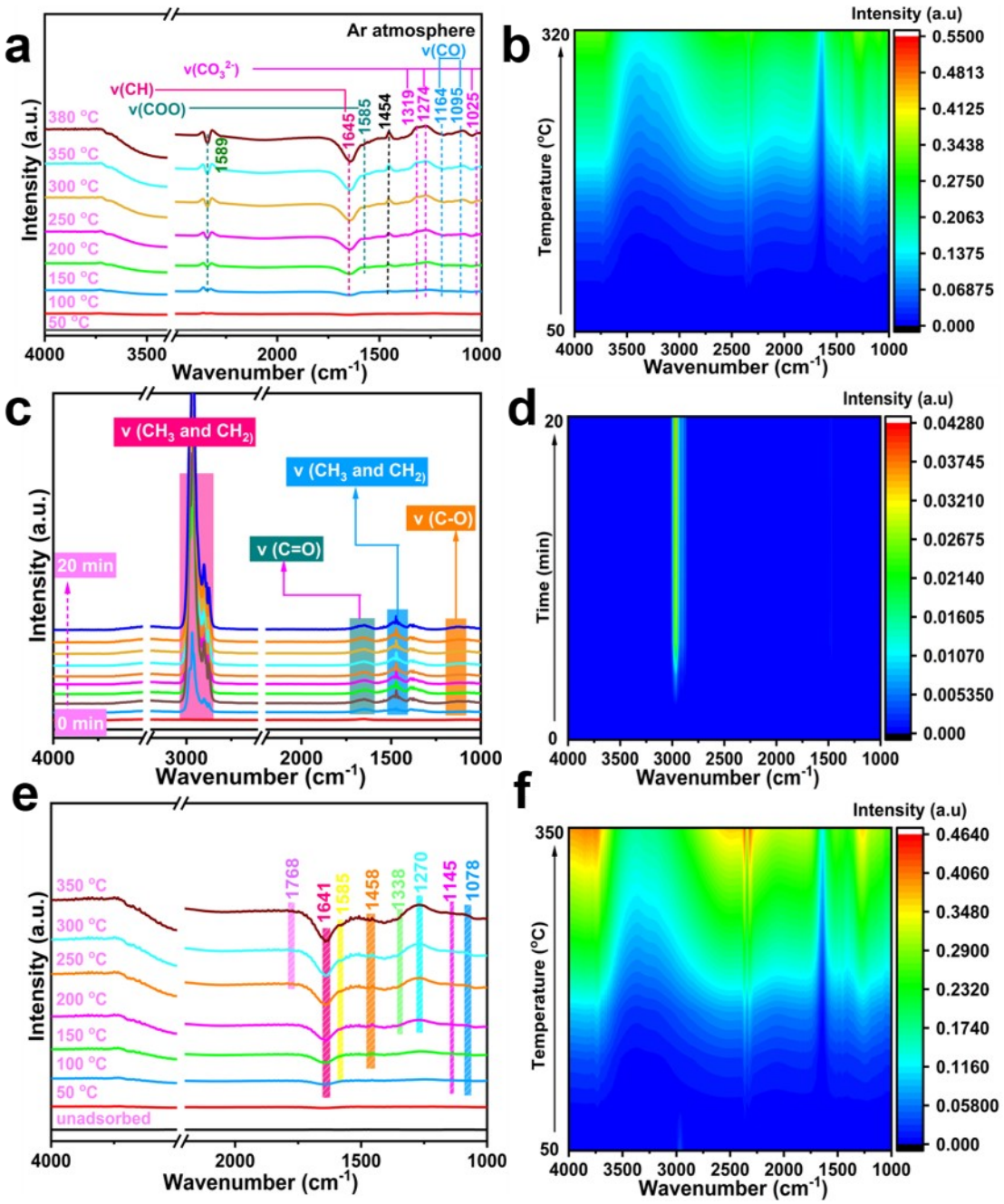

Fig. S15. (a and b) In-situ FTIR spectra for C_3H_8 adsorption of $CoMnO_x$ catalyst for different temperatures and (c-f) oxidation C_3H_8 at air on the $CoMnO_x$.